Delft University of Technology

Kerosene-H₂ blending effects on flame properties in a multi-fuel combustor

Dave, Kaushal; Link, Sarah; De Domenico, Francesca; Schrijer, Ferry; Scarano, Fulvio; Gangoli Rao, Arvind

Important note
To cite this publication, please use the final published version (if applicable).
Please check the document version above.

Kerosene-H$_2$ blending effects on flame properties in a multi-fuel combustor

Kaushal Dave [*] , Sarah Link , Francesca De Domenico , Ferry Schrijer , Fulvio Scarano ,
Arvind Gangoli Rao

Faculty of Aerospace Engineering, TU Delft, Kluyverweg 1, 2629 HS Delft, The Netherlands

ABSTRACT

In this study, the macroscopic properties of kerosene-H$_2$ blended flames are investigated in a multi-phase, multi-fuel combustor, focusing on the effects of increasing H$_2$ blending fractions. The non-reacting flow field of the swirl-stabilized combustor is characterized using PIV, and macro-structures in the flow and spray-swirl interactions are analyzed. Kerosene atomizers are tested to estimate variations in spray quality across different fuel blends. The changes in the optical properties of the flames are recorded using broadband chemiluminescence imaging while the changes in the acoustic emissions are recorded using a microphone. Results show that H$_2$ addition significantly alters the flame topology, transitioning from a lobed flame for pure kerosene to a single contiguous swirling flame for blended or pure H$_2$ cases. The flame luminosity decreases, with the emission color shifting from bright yellow (pure kerosene case) to dull yellow (multi-fuel cases) to a red-blue hue (pure H$_2$ case). These changes are attributed to variations in fuel distribution, heat release patterns, combustion mode, flame speed, and soot formation tendencies. The acoustic analysis reveals that a strong tonal behavior is observed under pure fuel conditions (prominent peaks at higher harmonics of 150 Hz) while broadband characteristics are exhibited under blended fuel conditions. The overall acoustic emissions in multi-fuel cases are reduced by ~80 % compared to pure H$_2$ and ~55 % compared to pure kerosene. This study highlights the effects of high levels of H$_2$ blending on flame dynamics and acoustic behavior in a multi-phase, multi-fuel combustor, offering valuable insights for the development of fuel-agnostic combustion systems.

1. Introduction

The aviation sector accounted for ~5 % of the anthropogenic causes of climate change in 2019 [1] with around one-third of this impact coming from direct CO$_2$ emissions [2]. The remaining contributions are from non-CO$_2$ effects, including NO$_X$, water vapor, aerosols, and contrails [2,3]. In the effort to decarbonize this sector, H$_2$ as a carbon-neutral energy carrier has emerged as an attractive option [4]. However, to date, the development of a fully H$_2$-fuelled aero-engine presents significant challenges [5,6], such as the need for new infrastructure development, scaling-up production of green-H$_2$, fuel supply chain robustness, and on-board H$_2$ storage and distribution [6,7]. Fuel-flexible hybrid engine technology, capable of handling kerosene-H$_2$ mixtures, represents an attractive interim strategy. Fuel-flexible aero-engines have the potential to mitigate several challenges associated with introducing H$_2$ as an energy source in aviation. By enabling greater versatility in fuel use, they can accelerate the adoption of H$_2$ and strongly contribute to the transition toward sustainable aviation.

However, the chemical properties of H$_2$ are significantly different from those of kerosene, and therefore, the injector design might require substantial modifications to enable fuel-agnostic operations.

From a combustion perspective, H$_2$ flames are characterized by a higher adiabatic flame temperature and a higher flame speed at any given equivalence ratio (φ) [8,9]. The increase in flame temperature makes H$_2$ flames susceptible to increased NO$_X$ formation while the increase in the flame speed makes the combustion system more susceptible to flashback.

The issue of increased flame temperature can be partly mitigated by leveraging the following two effects demonstrated when adding H$_2$ to the fuel mix. Firstly, H$_2$ requires less combustion air per unit of energy released compared to kerosene, implying that aero-engines using H$_2$ can be operated at leaner conditions. Secondly, the increased water vapor concentration in the product gases from H$_2$ combustion would result in a higher heat capacity of the exhaust gases. This can lower the required temperature at the combustor outlet for a given thrust setting [10,11]. Furthermore, while the increase in flame speed with H$_2$ blending can

Table 1
Summary of selected literature on kerosene-H_2 combustion studies.

Author Year	Fuel blends	R_h	Fuel injection	Method of investigation	Aspects Investigated
Hui et al., 2014 [19]	H_2/n-decane	0 – 44.2 %	Pre-vaporized, premixed	Chemical kinetics analysis	Ignition delay, laminar flame speed, extinction residence time, and emissions formation
Kozlov et al., 2020 [20]	H_2/n-decane	0 – 3.6 %	Pre-vaporized, partially and fully premixed	CFD simulations (RANS)	Emissions formation, temperature profiles
Alabas et al., 2024 [21]	H_2/Kerosene	0 – 50 %	Kerosene spray, Non-premixed H_2	CFD simulations (RANS)	Emissions formation, temperature profiles
Vance et al., 2024 [22]	H_2/n-dodecane	0 – 100 %	Pre-vaporized, premixed	1D & 2D laminar flame simulations	Effect on non-unity Lewis number of H_2 on flame stabilization.
Hiroyasu et al., 1980 [27]	H_2/Kerosene	0 – 100 %	Kerosene spray, non-premixed H_2	Experimental	Flammability limit, emission formation, flame properties
Juste, 2006 [23]	H_2/Kerosene	0 – 10.5 %	Kerosene spray, non-premixed H_2	Experimental	Emission formation
Frenillot et al., 2009 [24]	H_2/Kerosene	0 – 22 %	Pre-vaporized, premixed H_2	Experimental	Flammability limit, flame structure, emission formation
Burguburu et al. 2011 [25]	H_2/Kerosene	0 – 12 %	Kerosene spray, partially and fully premixed H_2	Experimental	Flammability limit, emission formation
Miniero et al., 2023 [26]	H_2/Kerosene	0 – 8 %	Kerosene spray, non-premixed H_2	Experimental	Flammability limit, emission formation, flame properties
Present study	H_2/Kerosene	0 – 100 %	Kerosene spray, premixed H_2	Experimental	Flame properties

be beneficial to flame stability at leaner conditions, the increased risk of flashback [12] is detrimental to engine operability and service life. Premixed swirl-stabilized combustors are particularly susceptible to this due to the presence of a low-velocity region at the center of the swirling jet. Reichel et al. [13] introduced the concept of using non-swirling axial air injection (AAI) to overcome this axial velocity deficit and thereby enhance flashback resistance. The approach has been followed in other studies [14,15], including the system developed at the Sustainable Aircraft Propulsion (SAP) laboratory of TU Delft for H_2 combustion research [16–18].

In recent years, the interest in fuel-flexible operations for aero-engines using kerosene/SAF and H_2 has grown, to overcome the challenges associated with H_2 as a fuel (e.g. Fokker Next Gen, CAVENDISH under Clean Aviation, Airbus ZEROe, etc.). This trend is reflected in the literature, with an increasing number of studies exploring this topic. While most focus on numerically investigating multi-phase, multi-fuel combustion [19–22], experimental research on this topic remains relatively limited. Most experimental studies [23–26] have focused on conditions where only a small fraction of the total fuel energy is derived from H_2, corresponding to a low hybrid ratio (R_h), which is defined as the ratio of H_2 energy to the total energy of the blend [27]. These studies primarily aim to evaluate the effects of H_2 as an additive on flammability limits, emissions, and combustion instabilities, rather than exploring fuel-flexible operation. A summary of selected literature on kerosene-H_2 multi-fuel combustion is provided in Table 1 including the type of analysis conducted, and the main aspects investigated.

To the authors' knowledge, the early study by Hiroyasu et al. [27] is the only work where the full range of mixtures (R_h: 0 – 100 %) of liquid kerosene and gaseous H_2 are tested in a modified gas turbine combustor. In this experiment, kerosene is injected via an air-blast atomizer that is modified to include a concentric annular slit for H_2 injection into the flame zone without any premixing. In this analysis, the authors focused on the cases where the thermal power and the total air flow entering the combustor were kept constant while the fuel composition was varied. It is reported that when $R_h < 10$ %, H_2 addition has a strongly positive effect on the flame stability (anchoring) and combustion efficiency while the soot and NO_X emissions measured in the exhaust gases only slightly increase. When R_h was increased within the range of 10 % to 50 %, a reduction in soot and NO_X emission is reported, with the combustion efficiency increasing to a plateau that starts at $R_h \sim 30$ %. Lastly, at $R_h > 50$ %, the flame was observed to behave like a pure H_2 flame without a significant change in NO_X and combustion efficiency, while the soot emission continued to reduce on account of a reduction in the share of hydrocarbon component in the fuel mixture.

Similarly, the other studies summarized in Table 1, despite using small blending fractions ($R_h \leq 25$ %), also highlight important trends regarding the effect of H_2 addition on kerosene combustion. Most analyses [23–25,27] report that CO emissions decrease as H_2 blending increases because H_2 replaces the carbonaceous fuel and enhances radical concentrations and fuel mixing, which promotes more complete CO oxidation to CO_2. In contrast, the impact of H_2 blending on NO_X emissions remains uncertain. While some studies [25] observe a positive correlation, others report negligible changes [23,24,27]. Chemical kinetics studies [28,29] suggest that the net effect depends on the H_2 injection method, which determines whether suppression via the prompt NO_X mechanism or an increase via the thermal NO_X mechanism dominates. Additionally, injecting H_2 significantly expands the envelope of stable combustion, especially under lean conditions. All experimental studies in Table 1 report improved flame stabilization and a lowered lean extinction limit (LEL) with H_2 addition.

It emerges from the above discussion that the existing literature on kerosene-H_2 blended combustion does not clearly identify technical limitations in blending a high fraction of H_2. Most experimental studies on this topic are limited to low R_h values and do not explicitly state the challenges in achieving stable combustion with pure H_2, pure kerosene, and intermediate blends. Additionally, the fact that these fuels are likely to be injected in different phases further complicates the design of an injection system. Insights into these blending limitations, if any, are important for advancing the development of next-generation fuel-agnostic engines. Furthermore, it is essential to investigate whether the combustor architectures used in state-of-the-art aero-engines can be adapted for future fuel-flexible systems. These two fundamental knowledge gaps motivate the present research of the authors. To fully understand kerosene-H_2 blending, it is essential to investigate the flame behavior at both macroscopic thermo-fluidic and thermo-chemical scales. The former is within the scope of this study. The objective of this work is to demonstrate the technical feasibility of utilizing a wide range of kerosene-H_2 blends in a novel multi-phase, multi-fuel combustor. This includes addressing the key research question: *"How do the macroscopic properties of flames in a multi-phase, multi-fuel combustor evolve with increasing H_2 blending fractions?"*

This is achieved in the present study by conducting reacting and non-reacting experiments in a novel optically accessible multi-phase multi-fuel combustion. The setup is designed to cover the entire range of fuel mixtures (R_h: 0–100 %) by retrofitting an existing technically premixed swirl-stabilized combustor with two kerosene atomizers. The non-reacting flow field is measured using Particle Image Velocimetry (PIV), while the impact of increasing H_2 fraction on the optical and

acoustic properties of the flames in the reacting experiments is monitored with a DSLR camera and microphone, respectively. The observed changes are qualitatively analyzed in terms of fuel distribution, heat release patterns, combustion mode, flame speed, and soot formation tendencies. This paper highlights the effects of H_2 blending on flame behavior and provides initial insights into the macroscopic properties of kerosene-H_2 blended flames, laying the groundwork for further exploration of multi-phase, multi-fuel combustion.

The structure of this article is as follows: Section 2 provides a detailed description of the experimental setup, including the hardware, layout, and operating conditions, as well as the visualization and measurement techniques used in this study. Section 3 presents the results, divided into two main parts: the non-reacting and reacting conditions. The non-reacting results include the combustor flow field and atomizer characterization, while the reacting conditions cover the optical and acoustic properties of the flames at varying R_h values. Finally, Section 4 summarizes the key findings of this study and discusses potential directions for future research.

2. Materials and methods

2.1. Multi-fuel combustor

The experimental setup is shown in Fig. 1. The baseline combustor is a technically premixed swirl-stabilized combustor for gaseous fuels that was retrofitted with the SIMPLEX atomizers. It comprises a swirl injector connected to a mixing tube (MT) that feeds the combustor with a technically premixed stream of gaseous reactants. The swirl injector used in this study is designed with helical vanes having an exit angle of $51.7°$ at its tip radius. The nominal swirl number, as defined in [30], at the swirler outlet is 0.7. The MT has a diameter of 24 mm and a length of 70 mm and is connected at the center of the base plate of the combustor. Two SIMPLEX-type atomizers (*Fluidics Instruments,* FI 0.15/80°/SF) are flush-mounted diametrically opposite on the base plate, at a distance of 38 mm from the central axis. A detailed view of the SIMPLEX injector assembly is shown in Fig. 1 (left insert). The combustor is a cylindrical quartz chamber, 400 mm long with a diameter of 148 mm and a wall thickness of 3.5 mm, providing optical access for flame imaging and laser diagnostics. It is connected to a flexible duct, 2 m in length and ~200 mm in diameter, which directs the exhaust gases to an off-site location. The base plate of the combustor also hosts a premixed methane/air *Honeywell, ZMI series* pilot burner which is used for remotely igniting the combustor during reacting flow experiments.

A majority of the combustion air is injected in the setup via the swirl air ports located upstream of the swirler while a small fraction of it is injected via the AAI port (inner diameter 8 mm), in the form of an axial jet, as shown in Fig. 1 (right insert). Gaseous fuel, in this case H_2, is injected into the MT via four fuel ports (inner diameter 3.2 mm) located immediately downstream of the swirler in a jet-in-swirling crossflow configuration. Liquid fuel, in this case, kerosene, is directly sprayed in the combustor via the SIMPLEX atomizers. Each atomizer is rated to a capacity of 9.5 g/min at an inlet pressure of 10 bar(g), producing an 80° solid cone spray pattern. The throughput of the atomizer under varying inlet pressures was measured under non-reacting conditions to determine its characteristic operating curve and estimate the spray quality using established empirical correlations for SIMPLEX-type atomizers. These results are discussed in more detail in the Section 3.1.2. Lastly, the flow of reactants is controlled via dedicated Bronkhorst mass flow controllers. The flow controllers used for gaseous reactants have a rated measurement uncertainty of ± 0.5 % reading $\pm$ 0.1 % full-scale, while that used for kerosene has a measurement uncertainty of ± 0.2 % reading $\pm$ 0.1 % full-scale.

2.2. Measured quantities

2.2.1. Flame luminance

Broadband chemiluminescence imaging of the flame is performed in the visible spectrum using a Nikon D7500 DSLR camera (23.5×15.7 mm^2 Red, Green, Blue (RGB) CMOS sensor, 21 MP, 4.2 μm pixel size) equipped with an AF-S DX NIKKOR 18–140mm telephoto lens. The camera is installed at a distance of ~680 mm from the center plane of the combustor, resulting in a field of view (FOV) of 228×152 mm^2 and a resolution of 24.5 pixels/mm. Video sequences of ~30 seconds duration are recorded at a resolution of 1920×1080 at 30 fps with a shutter speed of 1/800s. The instantaneous RGB images of the flames extracted from these video sequences are shown in Fig. 4.

Furthermore, the information in the blue channel of these images is isolated to obtain 8-bit grayscale images, which are used to evaluate the time-averaged topology of the flame zone shown in Fig. 5 . The blue pixels in most commercial color CMOS sensors have a peak quantum efficiency at ~440 nm, with a full width at half max (FWHM) of ~100 nm [31]. Thus, selecting only the information from the blue channel
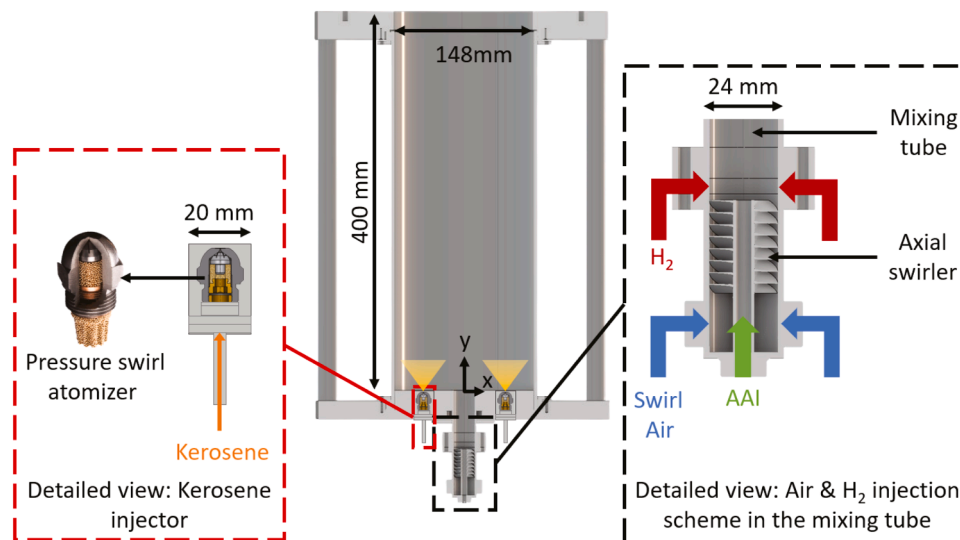

Fig. 1. Center: Schematic view of the multi-fuel combustor assembly showing different components including the swirl injector, MT and liquid fuel atomizers. Left: detail view of the pressure swirl atomizer used for injecting kerosene. Right: detail view of the swirler and the MT assembly showing the inlet ports for swirl air, AAI and H_2.

(390 – 490 nm) is a low-fidelity method for implementing a coarse filter for chemiluminescence signals. This range captures emissions peaks from CH* and C$_2$* radicals [32,33] which are key indicators of the re-action zone in hydrocarbon flames, while the emissions from other combustion products are largely excluded — specifically water vapor and soot as they emit predominantly at longer wavelengths. Although this approach sacrifices the spectral details, it provides a simplistic means to isolate reaction zone emissions for initial qualitative analysis.

2.2.2. Acoustic emissions

Acoustic emissions from the combustor are recorded with a microphone located at ~680 mm from the combustion chamber at a sampling rate of 44.1 kHz. The spectrum is evaluated using the p-Welch method [34]. In this analysis, 10-second audio samples were segmented into 100 ms intervals for Welch averaging. This segmentation yielded 4410 samples per segment, resulting in a frequency resolution of 10 Hz and a Nyquist frequency of 22 kHz in the power spectral density (PSD). Additionally, the sound emitted from the combustor under varying fuel conditions is also compared using the RMS value of the 10-second audio samples for each condition.

2.2.3. Flow field topology

The flow topology in non-reacting conditions is investigated using PIV. The swirling air and AAI streams were seeded with DEHS oil tracers of 0.9 μm diameter (peak of q3 size distribution) obtained using a PIV-TEC *PIVpart45* oil seeder. The tracers were illuminated by laser light from a Quantel *EverGreen 200* Nd:YAG laser (λ = 532 nm, 2×200 mJ, 15 Hz). The laser sheet thickness in the combustion chamber is ~3 mm. The light scattered from the tracers is detected by using a LaVision *Imager* sCMOS camera (16.6×14 mm^2 sensor, 5.5 MP, 6.5 μm pixel size). The camera is placed at a distance of ~1.2 m from the measurement plane and equipped with a 105 mm Nikkor lens, yielding a FOV of 198×167mm^2 and a spatial resolution of 12.9 pixels/mm. The raw particle images were processed using LaVision Davis 8 resulting in a vector pitch of 1.2 mm (32×32 pixel size and 50 % overlap). To mitigate the risk of accumulating combustible mixture in the setup during non-reacting experiments, the H$_2$ flow is replaced by a momentum-equivalent airflow keeping the ratio of fuel-stream momentum to air-stream momentum constant.

2.3. Experimental conditions

All reacting flow experiments are conducted at a constant power setting of 9 kW while maintaining the overall equivalence ratio, $\varphi_{overall}$ = 0.4. The experimental conditions, including the reactant mass flow rates, and resulting bulk velocity in the MT for the various fuel blends analyzed, are summarized in Table 2. In this study, the minimum atomization pressure requirement limits the maximum value of R$_h$ to 40 %. The combustor can operate at R$_h$ = 100 % by turning off the kerosene atomizers but blends with R$_h$ between 40 % and 100 % could not be tested. This limitation is discussed in more detail in Section 3.1.2.

3. Results and discussions

3.1. Non-reacting flow conditions

3.1.1. Combustor flow field

The velocity field in the axial plane of the combustor at comparable non-reacting conditions (i.e. Sw$_{geom}$ = 0.7 and AAI = 10 %) is shown in Fig. 2. The velocity and spatial data are presented in normalized form based on the bulk velocity in the MT (V$_b$ = 10.1 m/s) and the diameter of the MT as a reference. The flow topology is illustrated with the integrated streamlines. The swirling jet exits the MT and features a quasi-conical shape with a semi-aperture of ~35°, which delimits a toroidal recirculation on the outside (outer recirculation zone, ORZ). This region is observed to be anchored around foci located at y/D$_{MT}$ = ~1.5 and

Table 2
Flow rates of fuel (ṁ$_{H2}$ and ṁ$_{kero}$) and air (ṁ$_{air}$), resulting bulk-flow velocity in the MT (V$_b$), and the equivalence ratio of H$_2$/air mixture in the MT($\varphi_{MT,H2}$) for different fuel mixtures tested at constant power and overall equivalence ratio setting.

Power = 9kW and $\varphi_{overall}$ = 0.4					
R$_h$ (%)	ṁ$_{H2}$ (g/min)	ṁ$_{Kero}$ (g/min)	ṁ$_{air}$ (g/min)	V$_b$ (m/s)	$\varphi_{MT,H2}$ (-)
100 %	4.46	0.0	383	12.7	0.400
40 %	1.79	7.5	428	12.9	0.143
30 %	1.34	8.8	436	13.0	0.105
20 %	0.89	10.0	444	13.0	0.069
0 %	0.00	12.5	459	13.1	N/A

extends up to 3 diameters after which a forward flow condition is established. On the central axis, a large bulk of reverse flow is present (inner recirculation zone, IRZ) with maximum downward velocity (-0.4 V$_b$) near the exit (y/D$_{MT}$ = 1). The IRZ is fed with the recirculated mass flow by the two eddies with opposite circulation anchored around foci located at y/D$_{MT}$ = ~4.5.

The contour plot of the vertical velocity component illustrated in Fig. 2, helps to separate the regions of forward and reversed flow, with a black line highlighting the locus of zero vertical velocity. The interaction of the swirling jet with the IRZ and ORZ leads to the formation of the inner and outer shear layers (ISL and OSL respectively). Flames are usually located in low-velocity regions in ISL and OSL, where the local flow velocity matches the local flame speed.

The juxtaposition of the unperturbed spray plumes (80° solid cones) from the kerosene injectors with the velocity field is highlighted in purple. From this, it is expected that the kerosene spray is mostly injected into the ORZ, with some portion interacting with the OSL of the swirled jet. The placement of the SIMPLEX atomizers in this configuration is constrained by the geometric parameters of the baseline combustor. RANS-based CFD analysis of this configuration [35] showed inadequate mixing of the fuel and oxidizer in the combustor leading to the formation of fuel-rich regions in the ORZ. Future studies may apply these insights to optimize the injector placement to improve the mixing and distribution of the fuel spray within the combustor.

3.1.2. Atomizer characterization

The SIMPLEX atomizer was characterized under non-reacting conditions using kerosene. The injection pressure (ΔP) at the atomizer inlet was varied, and the corresponding mass flow rate was recorded. The pressure-flow rate relationship of the atomizer is presented in Fig. 3. Pressure measurements were conducted using a standard Bourdon tube gauge of class 2.5, with a total relative uncertainty of ±10 % accounting for the gauge's precision (±2 psi). Flow measurements exhibited a total propagated relative uncertainty of ±6 % within the experimental conditions outlined in Table 2.

It was observed that a minimum ΔP of 2 bar-gauge (bar-g) was needed to produce a spray, limiting the minimum flow rate of kerosene spray to 3.5 g/min (~2.5 kW) per injector. Consequently, fuel blends with R$_h$ values between 40 % and 100 % could not be covered in this study. This limitation can be overcome by employing atomizers rated for even smaller flow rates and/or by modifying the experimental setup to support higher overall power.

Using the experimentally determined pressure-flow rate curve, variations in spray quality at ambient conditions under different fuel blends were computed through well-established empirical correlations. The Sauter Mean Diameter (SMD or D$_{32}$), a standard metric representing the volume-to-surface area ratio of the spray, is conventionally used as a surrogate for spray quality in heat and mass transfer applications [36]. Its variation with ΔP is calculated using Eq. 1 [37] and is shown in Fig. 4.

$$SMD = 2.25 * \left(\frac{\sigma_L * \mu_L * \dot{m}_L}{\Delta P^2 * \rho_A} \right)^{0.25} \tag{1}$$
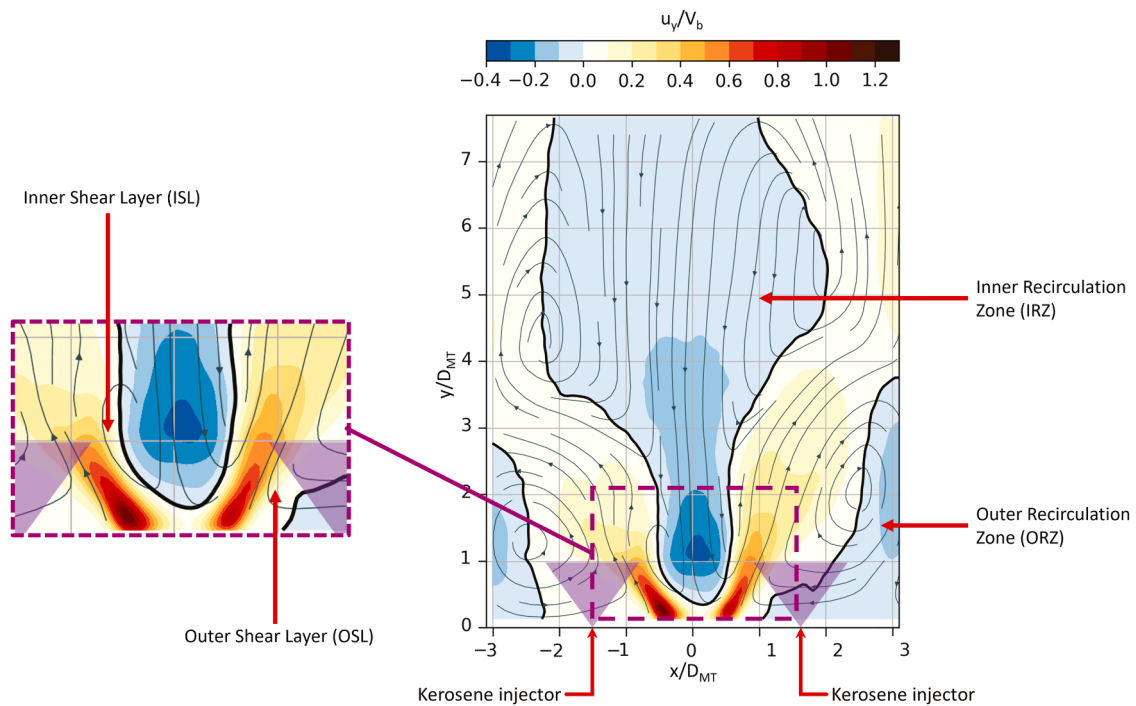
Fig. 2. Time averaged velocity field in the axial plane under non-reacting conditions. Integrated streamlines and colour contours of vertical velocity component superimposed with unperturbed spray plumes from the kerosene injectors is shown in the main image. A magnified view of the swirling jet emerging from the MT and the resulting ISL and OSL is shown in the left inset.
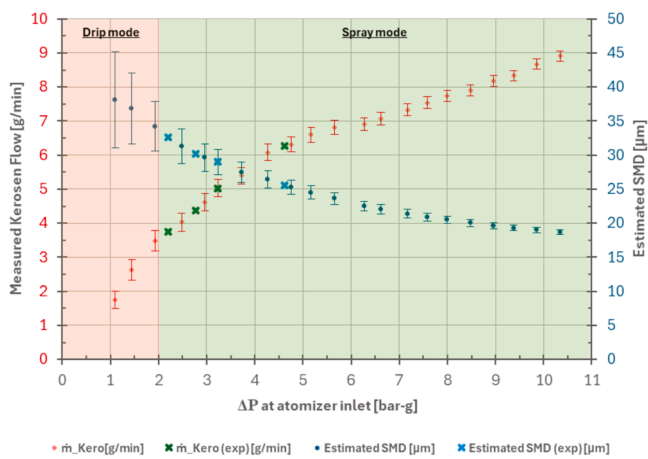

Fig. 3. Variation in the atomizer throughput and the estimated SMD of the resulting spray from the SIMPLEX atomizer at various injection pressures tested at ambient temperature.

where, σ_L, μ_L, $\dot{m}_L$, and ΔP are surface tension [N/m], dynamic viscosity in [kg/ms], mass flow rate [kg/s], and injection pressure [Pa] of kerosene at atomizer inlet respectively while ρ_A [kg/m^3] is the density of air.

Furthermore, based on the estimated SMD values, the droplet size distribution within the spray is determined assuming a Rosin-Rammler distribution. A spread parameter of 3.1 is used for these evaluations, as reported in [38]. The estimated values of SMD and droplet size distribution for the kerosene blends investigated are summarized in Table 3. The propagated uncertainty in these estimations was determined to be ±7 % within the range of experimental conditions explored in this study.

The expected variations in initial spray quality at injection across different cases are evident from the results shown in Table 3. As R_h increases, the fraction of kerosene energy and its mass flow must decrease,

which is achieved by reducing the ΔP at the atomizer inlet. However, this reduction in injection pressure causes the SMD of the spray to increase, leading to a deterioration in spray quality. Predicting the overall impact of this deterioration on the combustion properties is not straightforward, as the presence of H_2 in the fuel blends may counteract some of the adverse effects of reduced atomization quality to varying extents, as will be discussed in Section 3.2. Based on the values reported in Table 3, the estimated SMD of the spray increases by $\sim$20 % between the edge cases of pure kerosene and the fuel blend with $R_h = 40$ %, while the variation in the SMD between the blended cases is not very significant ($<$10 %).

3.2. Reacting flow conditions

3.2.1. Optical characteristics of the kerosene-H_2 flame

The investigation of multi-phase, multi-fuel flames in a practical combustor configuration provides valuable insights into the effects of kerosene-H_2 blending and uncovers novel aspects of the underlying physics of the combustion process. Fig. 4 presents a series of three instantaneous, time-uncorrelated flame images corresponding to the fuel mixtures detailed in Table 2. The images are arranged in rows to illustrate the temporal fluctuations in the observed flame structures, with the column representing the varying fuel conditions. A video compilation of these flames is included in the supplementary material of this article.

While the H_2 flame ($R_h = 100$ %) appears relatively steady, the multi-fuel flames exhibit visible fluctuations driven by the complex multi-phase, thermo-chemical interactions. As noted in [39], the local equivalence ratio inside a spray flame can vary significantly depending on the relative time scales of the underlying physical processes (transport, evaporation, and mixing) and the chemical processes involved in combustion. As a result, a spray flame could simultaneously display several flame structures. These have been broadly divided into three categories in the literature [40]: a) external combustion, with a continuous flame surface engulfing (partially or fully) the droplets and the evaporating gas phase (e.g. Fig. 4 Row 2, $R_h = 0$ %), b) group combustion, where droplet
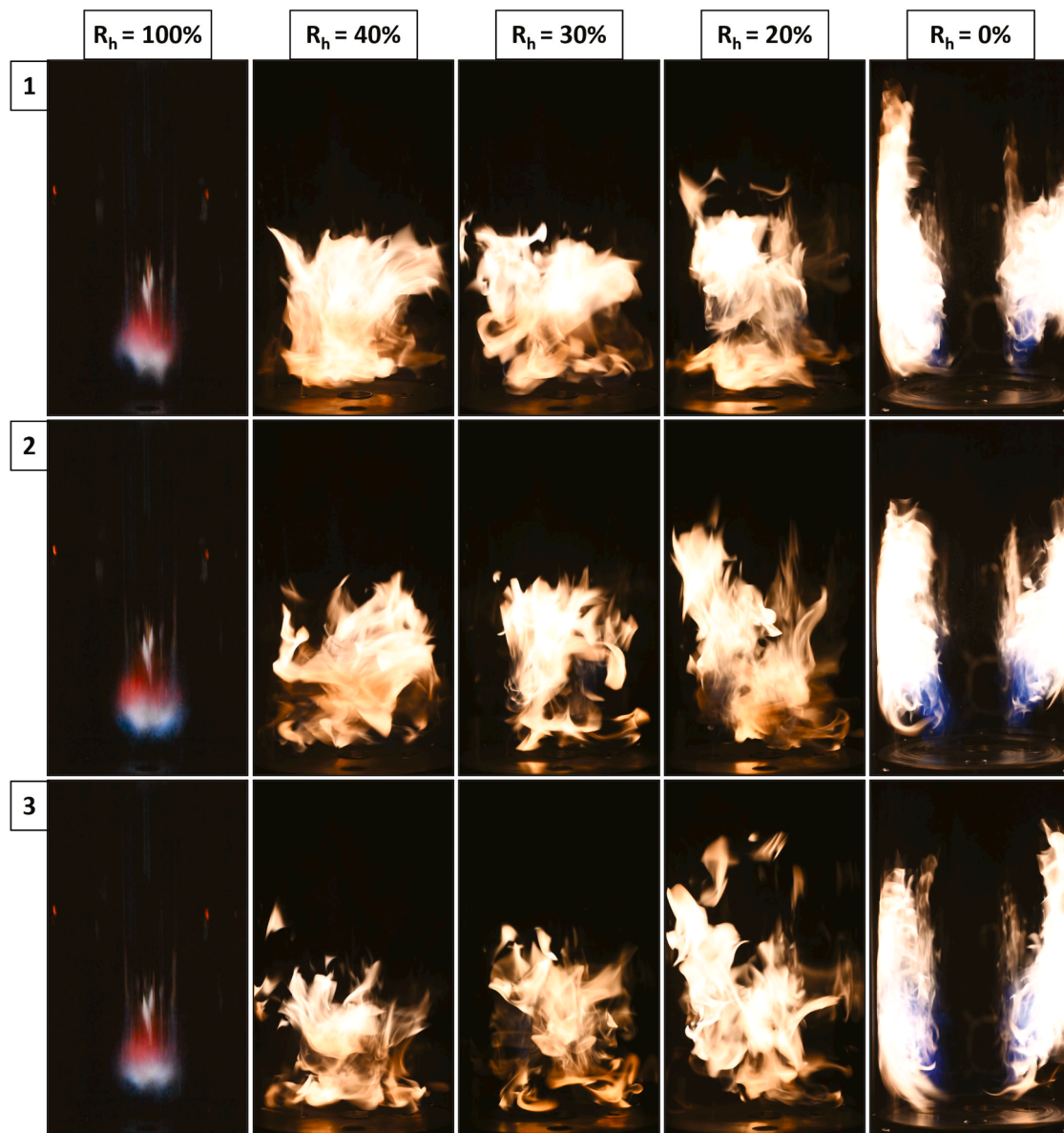
Fig. 4. Instantaneous snapshots of the multi-phase, multi-fuel flames with decreasing H_2 content (left to right), obtained at the conditions described in Table 2.

Table 3

Expected variation in spray parameters for the different kerosene blends investigated in the study.

R_h (%)	ΔP (bar-g)	SMD (μm)	X (μm)	$D_{0.05}$ (μm)	$D_{0.5}$ (μm)	$D_{0.95}$ (μm)
40 %	2.2	33	44	17	39	62
30 %	2.8	30	40	15	36	58
20 %	3.2	29	39	15	34	55
0 %	4.6	26	34	13	30	49

clusters are surrounded by separate flames (e.g. Fig. 4 Row 3, $R_h = 40$ %) and c) hybrid combustion mode, a combination of the previous two modes (e.g. Fig. 4 Row 3, $R_h = 20$ %).

Fig. 5 presents average flame images calculated from the blue component of approximately 800 uncorrelated instantaneous images captured by the DSLR camera as explained in Section 2.2.1. These time-averaged images effectively illustrate and compare the changes in the flame topology across varying fuel mixtures. The subsequent discussion focuses on examining the changes produced by different fuel mixtures

on the optical properties of the flame, particularly its appearance (color and luminosity) and its topology (shape and size).

Before proceeding with the flame image analysis, two minor aberrations in Fig. 5 should be noted. For $R_h = 30$ % and $R_h = 40$ %, a discontinuity in the intensity contours (pinching) appears in the region $1 < y/DMT < 3$, attributed to soot particle accumulation on the combustor wall. Additionally, the average image for $R_h = 20$ % shows an asymmetrical deflection to the top left corner, likely caused by fluctuations in the spray pattern from the two fuel nozzles. These aberrations, specific to the experiment, do not affect the analysis of flame topology across different fuel blends and are therefore considered within acceptable limits.

a. Flame color and luminosity

The flames under pure H_2 ($R_h = 100$ %), pure kerosene ($R_h = 0$ %), and blended cases, as depicted in Fig. 4, show distinctly different spectral characteristics (color). The pure H_2 flame exhibits a red-blue hue, typical of H_2 combustion under lean premixed conditions [41]. The pure kerosene flame, consistent with observations reported in the literature
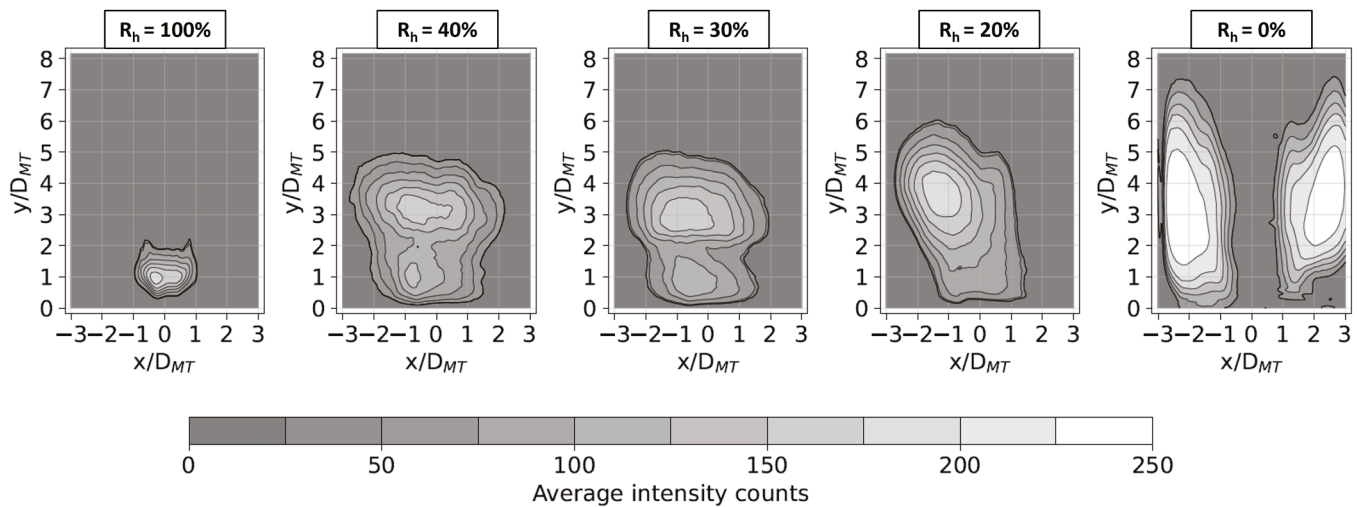
Fig. 5. Time-average intensity contours of the flame with varying levels of R_h.

[32], shows two distinct regions within each lobe (Fig. 4, Row 2, $R_h = 0$ %): 1) a blue-flame region immediately following the spray and 2) a yellow (sooty) flame region farther downstream in the combustor. The blue-flame region is ascribed to evaporating fuel droplets burning in an excess of oxidizer supplied from the mixing tube. The blue color arises from chemiluminescence emissions of CH*, and C_2* radicals. Soot chemistry, involving the formation of long-chain compounds, progresses relatively slowly, leaving the initial part of the flame free of the luminous appearance typical of sooty flames. As the reactants progress further downstream in the combustor, soot concentration is observed to increase, giving the flame a bright yellow appearance.

In contrast, the flames under blended fuel conditions ($R_h = 20$ %, 30 %, and 40 %) differ from both pure fuel cases, exhibiting a sooty (dull yellow) appearance from the outset, as shown in Fig. 4. The absence of the initial blue-flame region in the blended cases can be attributed to two factors. First, the relative concentration of oxidizer in the ORZ may be lower because a part of it would get consumed by the premixed H_2. Second, previous studies [42,43] have reported that the sooting tendency of hydrocarbon flames shows a positive correlation with reactant temperature. It is shown in [35] that, in comparison to pure kerosene flame, the temperature in the ORZ is significantly higher under blended conditions (due to the heat released from H_2 combustion reactions). This increase in local availability of heat near the fuel injectors likely enhances the evaporation of fuel droplets, causing combustion to occur under fuel-rich conditions in the ORZ which moves the soot inception point closer to the fuel injection location.

Furthermore, a variation in luminosity is seen among the kerosene cases by observing Fig. 4 and Fig. 5. As R_h decreases, there is a discernable increase in flame luminosity with the flames changing from a dull yellow appearance under blended conditions to a bright yellow appearance under the pure kerosene case. This change is most prominently seen when comparing Fig. 4 Row 2, $R_h = 20$ % with Fig. 4 Row 2, $R_h = 0$ %. This trend correlates well with the expected reduction in soot production with H_2 addition as previously reported in the literature [27, 44–46]. This reduction is primarily attributed to two effects: the substitution of hydrocarbon fuel with H_2 and the increased availability of free radicals in the combustor, promoting more complete oxidation as R_h rises.

It is important to acknowledge the potential influence of the line-of-sight effect inherent to the DSLR images employed in this study. This aspect may partly contribute to the noted variations in luminosity, particularly in the case of pure kerosene where flames are confined to a smaller section of the combustion chamber. Such confinement could cause the flame to appear more intense due to signal integration along the line of sight. Nevertheless, quantitative measurements reported in

the literature [27,44–46] support the hypothesis that the observed change in flame luminosity arises from the reduced soot formation tendency as the R_h value in the fuel mixture increases.

b. Flame topology

A clear difference in flame topologies can be observed in Figs. 4 and 5. In all cases with $R_h > 0$ %, a single contiguous flame zone is observed, swirling about the central axis. In contrast, for pure kerosene ($R_h = 0$ %), lobed flame zones with two distinct lobes/wings are evident. Similar changes in flame shapes are also seen in the results of the RANS simulations reported in [35]. A change in fuel distribution in the combustor and the resulting changes in the heat release pattern are considered the likely cause of this effect. At the outset of this discussion, a simplifying assumption is made: the multi-fuel cases are treated as a superposition of a kerosene spray flame and a swirling H_2 flame, with their interaction limited to heat transfer. This assumption is based on the premise that the physical characteristics of the flame, such as topology, are primarily influenced by thermo-fluidic effects in the combustor, rather than the chemical effects of H_2 blending.

Fig. 5 distinctly shows that even the smallest amount of H_2 tested in the study significantly alters the topology of the pure kerosene spray flame, transitioning it from a lobed structure stabilizing over the two injectors to a single swirling flame zone. However, as reported in Table 3, the estimated spray quality is comparable in both these cases, with the SMD showing only a slight increase in the multi-fuel case. This suggests that, under similar flow conditions in the combustor, the fuel droplets in the pure kerosene case would be expected to track the flow more effectively than those in the multi-fuel case. Considering the injection location of the fuel spray (refer to Fig. 2), droplets that can track the flow more effectively can be expected to be entrained in the toroidal recirculation region formed by the ORZ, and result in a more swirling flame structure. However, the actual flame topology observed during the experiment shows a contrary trend and therefore, the initial spray quality alone cannot explain the observed trends.

The changes in flame topology can be better explained by considering the effect of H_2 blending on the heat release pattern and droplet transport. In the multi-fuel cases, H_2 is injected into the MT and enters the combustor premixed with air, resulting in the formation of a central flame that is likely anchored in the ISL and OSL. The hot product gases from this flame are entrained into the recirculation zones, thereby enhancing the evaporation and mixing of kerosene droplets injected into this region. In contrast, for the pure kerosene case ($R_h = 0$ %), the swirling jet lacks premixed gaseous fuel, and thus, no central flame is formed. The temperature fields reported in [35] support this reasoning,

showing a temperature difference of several hundred degrees between the blended and pure kerosene cases. This strongly suggests that the fuel droplets in the multi-fuel cases are met with higher temperatures after their injection, which would promote faster evaporation compared to those in the pure kerosene case. This increased evaporation rate compensates for the initial differences in spray quality across the different cases and reduces the overall size distribution in the multi-fuel cases after injection. It is well-known in literature [47,48] that the tracking effectiveness of droplets entrained in multi-phase flow increases as their size decreases. Consequently, the smaller fuel droplets in the multi-fuel cases follow the swirling flow in the ORZ more effectively and get entrained in the toroidal recirculation zone. In contrast, the relatively slow evaporating droplets in the pure kerosene case are less likely to get entrained in the ORZ and are instead transported downstream into the combustor, resulting in the lobed/winged flame topology in the pure kerosene case, as shown in Fig. 4 and Fig. 5.

Finally, the last visible change that can be observed in the flames under different fuel blends is the variation in flame height, as illustrated in Fig. 5. The spatial dimensions of the average flames are normalized using the diameter of the MT. The flame height for the pure H_2 case (R_h = 100 %) is observed to be ~2 D_{MT}, while the pure kerosene case (R_h = 0 %) reaches ~8 D_{MT}. The heights of the multi-fuel flames fall in the intermediate range of 5 – 6 D_{MT}. The ongoing discussion on the changes in the heat release pattern and droplet transport within the combustor is also applicable here and it is partly responsible for this variation. The increased entrainment of fuel droplets into the ORZ under the multi-fuel cases results in the flames being confined to a shorter region of the combustor. In contrast, in the pure kerosene case, the fuel droplets are transported further downstream in the combustor along with the expanding jet, resulting in a taller flame structure. The variation in flame height is partly also caused by higher mixture consumption speeds due to H_2 blending [8,9]. Although it is difficult to assess the level of pre-mixing in a multi-phase, multi-fuel setup, there is certainly an increase in the effective burning speed as the R_h value increases, primarily due to the partial mixing and preheating of a portion of the liquid fuel undergoing spray combustion.

3.2.2. Acoustic characteristics of the kerosene-H_2 flame

In addition to the changes in the flame topology, it was also found that variations in fuel mixture affect the acoustic emissions of the combustor. Table 4 lists the variation in the RMS amplitude calculated from 10-second-long audio signals under varying fuel conditions. To highlight the variations in intensity across different cases, the results are expressed as relative sound pressure levels in decibels (Δ dB SPL), calculated using Eq. 2. The pure H_2 case was chosen as the reference because it demonstrated the highest RMS amplitude.

$$\Delta\, SPL_{R_h} = 20 * \log_{10}\left(\frac{RMS_{R_h}}{RMS_{R_h=100\,\%}}\right) \qquad (2)$$

It is observed that the pure kerosene case (R_h = 0 %) exhibited the second-highest acoustic intensity. The reduction in this case is ~3.8 dB and represents a decrease of 58 % in the acoustic intensity in comparison to the pure H_2 case. Moreover, a decrease of ~7.4 dB (80 %) relative to the pure H_2 case and ~3.6 dB (55 %) relative to pure kerosene was observed when the combustor was operated in a multi-fuel regime.

Table 4
Comparison of the RMS amplitude and the relative intensity level of the recorded acoustic signal measured over a duration of 10 seconds.

R_h [%]	RMS amplitude [arb. units]	Relative Intensity [Δ dB SPL]
100 %	0.87	0.00 (Reference)
40 %	0.38	-7.12
30 %	0.37	-7.49
20 %	0.36	-7.67
0 %	0.56	-3.84

Amongst the three multi-fuel cases, an increasing trend in the RMS amplitude is observed as R_h increases.

The reduction in the RMS amplitude of the acoustic emissions can be understood further by comparing the power spectrum in the frequency domain. Fig. 6 shows the relative power spectral density (PSD) for the pure H_2 (R_h = 100 %), pure kerosene (R_h = 0 %) and blended fuel case (R_h = 40 %). Additionally, a compilation of audio samples for these cases is included in the supplementary material of this article. Again, the results are shown relative to the loudest tone observed in the pure H_2 case at 300 Hz frequency. In this case, a reduction of 10 dB would indicate a 10-fold decrease in acoustic intensity compared to the reference value.

The acoustic spectrum originating from the combustor exhibits noticeable changes under different fuel conditions. For pure H_2 (R_h = 100 %) and pure kerosene (R_h = 0 %), a strong tonal signature is observed, with prominent peaks at the higher harmonics of 150 Hz. This fundamental frequency is likely associated with the resonant frequency of the combined system of the combustion chamber and exhaust duct, approximated as a 2.4 m long open pipe.

In contrast, these tonal components are significantly suppressed (10–20 dB reduction) in the multi-fuel cases, particularly at 300, 900, and 1500 Hz. While the broadband amplitude is slightly higher in the multi-fuel cases (evidenced by the blue line (R_h = 40 %) generally lying above the green (R_h = 100 %) and brown (R_h = 0 %) lines in Fig. 6), the suppression of tonal peaks markedly reduces the overall RMS amplitude of the signal, as shown in Table 4.

A similar trend was observed in [24] where it is reported that introducing a small fraction of H_2 suppresses the low-frequency tones observed in the case of pure kerosene operation. The underlying cause for these observed changes in the acoustic emissions of the combustor (strong tonality under pure fuel cases vs broadband emissions in blended fuel cases) is not fully understood and deserves future investigations.

4. Conclusion

This study investigates the macroscopic properties of kerosene-H_2 blended flames in a multi-phase, multi-fuel combustor, with a focus on exploring the effects of increasing R_h on flame behavior. This is achieved through a series of reacting and non-reacting experiments. The baseline flow field under non-reacting conditions is characterized using PIV, revealing the outer and inner recirculating regions and potential spray-swirl interactions. Additionally, atomizer performance is also assessed under non-reacting conditions to estimate variations in spray quality across different fuel blends. The flame structure is visualized through imaging, and acoustic emissions are recorded using a microphone. While practical limitations on the flow rate of the atomizers restricted the
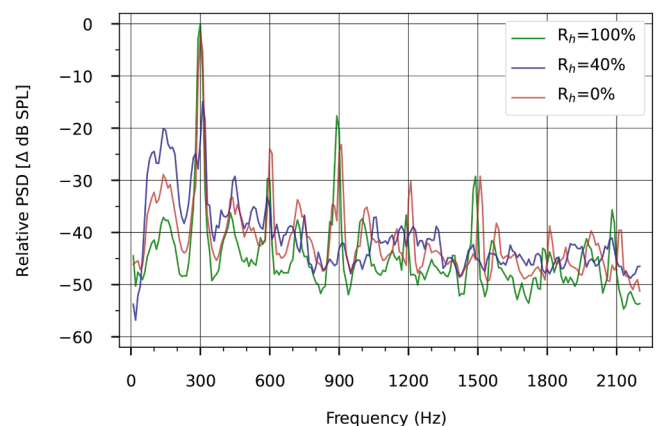

Fig. 6. Relative power spectral density of the acoustic signal recorded during operations of the combustor at R_h = 100 %, 40 % and 0 %. The reference SPL level is taken at R_h = 100 % and frequency = 300 Hz.

maximum value of R_h to 40 %, the study demonstrates that a full range of kerosene-H2 blends can be tested within the present configuration. The findings underscore the distinctly different flame properties observed under pure H_2, pure kerosene, and blended fuel regimes.

From a combustion perspective, faster evaporation and mixing of kerosene are promoted by increasing R_h, leading to changes in fuel transport within the combustor and ultimately in the flame topology. The addition of H_2 also impacts the sooting tendency of the flame, altering the location of soot inception (as evidenced by color changes) and reducing soot formation (indicated by changes in flame luminance).

Furthermore, the acoustic analysis shows that pure fuel conditions exhibit distinct tonal behavior, while blended fuels display broadband characteristics. In the multi-fuel regime, overall acoustic emissions are reduced by 80 % compared to pure H_2 and by 55 % compared to pure kerosene. Despite a slight increase in broadband noise levels, this reduction is primarily due to the suppression of tonal components at 300, 900, and 1500 Hz. The mechanisms underlying these changes remain unclear and warrant further investigation.

This study provides novel insights into the effects of high levels of H_2 blending on flame behavior and acoustic emissions in a multi-phase, multi-fuel combustor, an area that remains underexplored in the literature. Future work will focus on further exploring the interactions between kerosene droplets and H_2 flames, and understanding the underlying mechanisms driving the observed changes in flame topology and acoustic signature.

CRediT authorship contribution statement

Kaushal Dave: Writing – review & editing, Writing – original draft, Visualization, Methodology, Investigation, Data curation, Conceptualization. **Sarah Link:** Writing – review & editing, Investigation. **Francesca De Domenico:** Writing – review & editing, Supervision, Conceptualization. **Ferry Schrijer:** Writing – review & editing, Supervision. **Fulvio Scarano:** Writing – review & editing, Supervision. **Arvind Gangoli Rao:** Writing – review & editing, Supervision, Funding acquisition, Conceptualization.

Declaration of competing interest

The authors declare that they have no known competing financial interests or personal relationships that could have appeared to influence the work reported in this paper.

Supplementary materials

Supplementary material associated with this article can be found, in the online version, at doi:10.1016/j.jfueco.2025.100139.

Data availability

Data will be made available on request.

References

[1] Rao AG, Yin F, Werij HGC. Energy transition in aviation: the role of cryogenic fuels. Aerospace 2020 2020;7(7):181. https://doi.org/10.3390/AEROSPACE7120181. 181.

[2] Lee DS, Fahey DW, Skowron A, Allen MR, Burkhardt U, Chen Q, Doherty SJ, Freeman S, Forster PM, Fuglestvedt J, Gettelman A, De León RR, Lim LL, Lund MT, Millar RJ, Owen B, Penner JE, Pitari G, Prather MJ, Sausen R, Wilcox LJ. The contribution of global aviation to anthropogenic climate forcing for 2000 to 2018. Atmos Environ 2021;244:117834. https://doi.org/10.1016/J.ATMOSENV.2020.117834.

[3] Megill L, Deck K, Grewe V. Alternative climate metrics to the global warming potential are more suitable for assessing aviation non-CO2 effects. Commun Earth Environ 2024 2024;5(1 5):1–9. https://doi.org/10.1038/s43247-024-01423-6.

[4] IEA. The Future of Hydrogen. Seizing today's opportunities. OECD; 2019. https://doi.org/10.1787/1e0514c4-en.

[5] G. Corchero, J.L. Montañés, An approach to the use of hydrogen for commercial aircraft engines, 10.1243/095441005×9139 219 (2005) 35–44. https://doi.org/10.1243/095441005×9139.

[6] Degirmenci H, Uludag A, Ekici S, Karakoc TH. Challenges, prospects and potential future orientation of hydrogen aviation and the airport hydrogen supply network: A state-of-art review. Prog Aerosp Sci 2023;141:100923. https://doi.org/10.1016/J.PAEROSCI.2023.100923.

[7] Baroutaji A, Wilberforce T, Ramadan M, Olabi AG. Comprehensive investigation on hydrogen and fuel cell technology in the aviation and aerospace sectors. Renew Sustain Energy Rev 2019;106:31–40. https://doi.org/10.1016/J.RSER.2019.02.022.

[8] Xu C, Wang Q, Li X, Liu K, Liu W, Oppong F, Sun ZY. Effect of hydrogen addition on the laminar burning velocity of n-decane/air mixtures: experimental and numerical study. Int J Hydrogen Energy 2022;47:19263–74. https://doi.org/10.1016/J.IJHYDENE.2022.03.290.

[9] Oppong F, Li X, Xu C, Li Y, Wang Q, Liu Y, Qian L. Investigation on n-decane-hydrogen laminar combustion characteristics using the constant volume combustion method. Int J Hydrogen Energy 2024;53:1350–60. https://doi.org/10.1016/J.IJHYDENE.2023.11.361.

[10] Derakhshandeh P, Ahmadi A, Dashti R. Simulation and technical-economic-environmental optimization of the General Electric GE90 hydrogen turbofan engine. Int J Hydrogen Energy 2021;46:3303–18. https://doi.org/10.1016/J.IJHYDENE.2020.10.182.

[11] X. Wang, A. He, Z. Hu, Transient modeling and performance analysis of hydrogen-fueled aero engines, processes 2023, Vol. 11, 423 11 (2023) 423. https://doi.org/10.3390/PR11020423.

[12] Sayad P, Schönborn A, Klingmann J. Experimental investigation of the stability limits of premixed syngas-air flames at two moderate swirl numbers. Combust Flame 2016;164:270–82. https://doi.org/10.1016/J.COMBUSTFLAME.2015.11.026.

[13] Reichel TG, Terhaar S, Paschereit O. Increasing flashback resistance in lean premixed swirl-stabilized hydrogen combustion by Axial air injection. J Eng Gas Turbine Power 2015;137. https://doi.org/10.1115/1.4029119.

[14] Stathopoulos P, Kuhn P, Wendler J, Tanneberger T, Terhaar S, Paschereit CO, Schmalhofer C, Griebel P, Aigner M. Emissions of a wet premixed flame of natural gas and a mixture with hydrogen at high pressure. J Eng Gas Turbine Power 2017; 139:611–67. https://doi.org/10.1115/1.4034687.

[15] Hatem FA, Alsaegh AS, Al-Faham M, Valera-Medina A, Chong CT, Hassoni SM. Enhancing flame flashback resistance against combustion induced vortex breakdown and boundary layer flashback in swirl burners. Appl Energy 2018;230: 946–59. https://doi.org/10.1016/J.APENERGY.2018.09.055.

[16] Link S, Dave K, Eitelberg G, Rao AG, de Domenico F. The influence of the confinement ratio on the precessing vortex core dynamics in a counter-rotating dual swirler. In: Proceedings of the ASME Turbo Expo 3B-2023; 2023. https://doi.org/10.1115/GT2023-101678.

[17] G. Ferrante, L. Doodeman, A.G. Rao, I. Langella, LES of hydrogen-enriched methane flames in a lean-burn combustor with axial air injection, proceedings of the ASME Turbo Expo 3B-2023 (2023). https://doi.org/10.1115/GT2023-103006.

[18] Link S, Dave K, de Domenico F, Rao AG, Eitelberg G. Experimental analysis of dual-fuel (CH4/H2) capability in a partially-premixed swirl stabilized combustor. Int J Hydrogen Energy 2025;101:427–37. https://doi.org/10.1016/j.ijhydene.2024.12.286.

[19] Hui X, Zhang C, Xia M, Sung CJ. Effects of hydrogen addition on combustion characteristics of n-decane/air mixtures. Combust Flame 2014;161:2252–62. https://doi.org/10.1016/J.COMBUSTFLAME.2014.03.007.

[20] Kozlov VE, Titova NS, Torokhov SA. Numerical study of the effect of hydrogen or syngas additions to n-decane on the harmful substance emission from a homogeneous combustion chamber. Russian J Phys Chem B 2020;14:395–406. https://doi.org/10.1134/S1990793120030082.

[21] Alabaş HA, Çeper BAlbayrak. Effect of the hydrogen/kerosene blend on the combustion characteristics and pollutant emissions in a mini jet engine under CDC conditions. Int J Hydrogen Energy 2024;52:1275–87. https://doi.org/10.1016/J.IJHYDENE.2023.05.146.

[22] Vance FH, Nicolai H, Hasse C. A numerical investigation into the stabilization of hydrogen enriched n-dodecane premixed flames. Int J Hydrogen Energy 2024;56: 611–20. https://doi.org/10.1016/J.IJHYDENE.2023.12.219.

[23] Juste GL. Hydrogen injection as additional fuel in gas turbine combustor. Evaluation of effects. Int J Hydrogen Energy 2006;31:2112–21. https://doi.org/10.1016/J.IJHYDENE.2006.02.006.

[24] Frenillot JP, Cabot G, Cazalens M, Renou B, Boukhalfa MA. Impact of H2 addition on flame stability and pollutant emissions for an atmospheric kerosene/air swirled flame of laboratory scaled gas turbine. Int J Hydrogen Energy 2009;34:3930–44. https://doi.org/10.1016/J.IJHYDENE.2009.02.059.

[25] Burguburu J, Cabot G, Renou B, Boukhalfa A, Cazalens M. Comparisons of the impact of reformer gas and hydrogen enrichment on flame stability and pollutant emissions for a kerosene/air swirled flame with an aeronautical fuel injector. Int J Hydrogen Energy 2011;36:6925–36. https://doi.org/10.1016/J.IJHYDENE.2011.01.185.

[26] Miniero L, Pandey K, De Falco G, D'Anna A, Noiray N. Soot-free and low-NO combustion of Jet A-1 in a lean azimuthal flame (LEAF) combustor with hydrogen injection. Proceed Combust Instit 2023;39:4309–18. https://doi.org/10.1016/J.PROCI.2022.08.006.

[27] Hiroyasu H, Arai M, Kadota T, Yoso J. An experimental study on kerosene-hydrogen hybrid combustion in a gas turbine combustor. Bullet JSME 1980;23:1655–62. https://doi.org/10.1299/JSME1958.23.1655.

[28] Naha S, Aggarwal SK. Fuel effects on NOx emissions in partially premixed flames. Combust Flame 2004;139:90–105. https://doi.org/10.1016/J.COMBUSTFLAME.2004.07.006.

[29] Naha S, Briones AM, Aggarwal SK. Effect of Fuel blends on pollutant emissions in flames. Combust Sci Technol 2004;177:183–220. https://doi.org/10.1080/00102200590883822.

[30] J.M. Beér, Chigier N.A., Combustion Aerodynamics, Krieger, 1983.

[31] Skorka O, Kane P, Ispasoiu R. Color correction for RGB sensors with dual-band filters for in-cabin imaging applications. Electron Imag 2019;31:1–8. https://doi.org/10.2352/ISSN.2470-1173.2019.15.AVM-046.

[32] Nakamura M, Nishioka D, Hayashi J, Akamatsu F. Soot formation, spray characteristics, and structure of jet spray flames under high pressure. Combust Flame 2011;158:1615–23. https://doi.org/10.1016/J.COMBUSTFLAME.2010.12.033.

[33] Vogel M, Bachfischer M, Kaufmann J, Sattelmayer T. Experimental investigation of equivalence ratio fluctuations in a lean premixed kerosene combustor. Exp Fluids 2021;62. https://doi.org/10.1007/s00348-021-03197-5.

[34] Welch PD. The use of fast fourier transform for the estimation of power spectra: A method based on time averaging over short, modified periodograms. IEEE Transa Audio Electroac 1967;15:70–3. https://doi.org/10.1109/TAU.1967.1161901.

[35] Palanti L, Mazzei L, Bianchini C, Link S, Dave K, de Domenico F, Rao AG. CFD-based scouting for the design of a multi-fuel kerosene/hydrogen atmospheric burner. ICAS Proceedings. 2024. https://www.icas.org/icas_archive/icas2024/data/papers/icas2024_0432_paper.pdf.

[36] Rashad M, Yong H, Zekun Z. Effect of geometric parameters on spray characteristics of pressure swirl atomizers. Int J Hydrogen Energy 2016;41:15790–9. https://doi.org/10.1016/J.IJHYDENE.2016.04.037.

[37] A.H. Lefebvre, V.G. McDonell, Atomization and sprays, 2017. https://doi.org/10.1201/9781315120911.

[38] Domingo-Alvarez P, Bénard P, Moureau V, Lartigue G, Grisch F. Impact of spray droplet distribution on the performances of a Kerosene Lean/premixed injector. Flow Turbul Combust 2020;104:421–50. https://doi.org/10.1007/s10494-019-00073-5.

[39] Jenny Patrick, Roekaerts Dirk, Beishuizen Nijso. Modeling of turbulent dilute spray combustion. Elsevier Prog Energy Combust Sci 2012;38:846–87. https://doi.org/10.1016/j.pecs.2012.07.001.

[40] Reveillon J, Vervisch L. Analysis of weakly turbulent dilute-spray flames and spray combustion regimes. J Fluid Mech 2005;537:317–47. https://doi.org/10.1017/S0022112005005227.

[41] Schefer RW, Kulatilaka WD, Patterson BD, Settersten TB. Visible emission of hydrogen flames. Combust Flame 2009;156:1234–41. https://doi.org/10.1016/J.COMBUSTFLAME.2009.01.011.

[42] Zhang Z, Zhou L, He X, Chen L, Wei H. Effect of preheating air temperature on sooting tendency in laminar co-flow diffusion flame of n-heptane. Combust Flame 2023;251:112719. https://doi.org/10.1016/J.COMBUSTFLAME.2023.112719.

[43] Chu C, Zaher MH, Thomson MJ. The temperature dependence of soot formation in laminar coflow aromatic flames. Combust Flame 2022;241:112074. https://doi.org/10.1016/J.COMBUSTFLAME.2022.112074.

[44] Pandey P, Pundir BP, Panigrahi PK. Hydrogen addition to acetylene–air laminar diffusion flames: studies on soot formation under different flow arrangements. Combust Flame 2007;148:249–62. https://doi.org/10.1016/J.COMBUSTFLAME.2006.09.004.

[45] Wei M, Liu J, Guo G, Li S. The effects of hydrogen addition on soot particle size distribution functions in laminar premixed flame. Int J Hydrogen Energy 2016;41:6162–9. https://doi.org/10.1016/J.IJHYDENE.2015.10.022.

[46] Wu R, Song X, Wei J, Bai Y, Wang J, Lv P, He T, Parvez AM, Yu G. Hydrogen addition in methane-oxygen laminar inverse diffusion flames: A study focused on free radical chemiluminescence and soot formation. Int J Hydrogen Energy 2024;54:1029–39. https://doi.org/10.1016/J.IJHYDENE.2023.11.256.

[47] Hardalupas Y, Taylor AMKP, Whitelaw JM. Particle dispersion in a vertical round sudden-expansion flow. Philos Trans Royal Soc London. Series A: Phys Eng Sci 1992;341:411–42. https://doi.org/10.1098/RSTA.1992.0110.

[48] Apte SV, Mahesh K, Moin P, Oefelein JC. Large-eddy simulation of swirling particle-laden flows in a coaxial-jet combustor. Int J Multi Flow 2003;29:1311–31. https://doi.org/10.1016/S0301-9322(03)00104-6.